The impact of pore-throat shape evolution during dissolution on carbonate rock permeability: pore network modelling and experiments

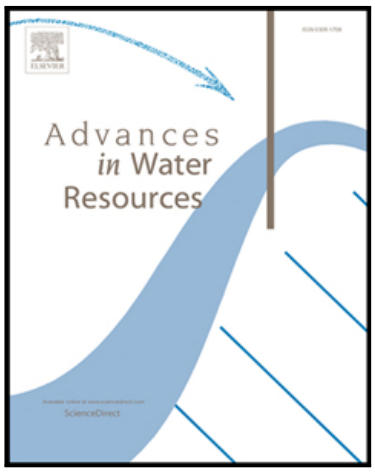

The impact of pore-throat shape evolution during dissolution on carbonate rock permeability: pore network modelling and experiments

Priyanka Agrawal , Arjen Mascini , Tom Bultreys , Hamed Aslannejad , Mariëtte Wolthers , Veerle Cnudde , Ian B. Butler , Amir Raoof

PII: S0309-1708(21)00146-9
DOI: https://doi.org/10.1016/j.advwatres.2021.103991
Reference: ADWR 103991

To appear in: *Advances in Water Resources*

Received date: 10 March 2021
Revised date: 31 May 2021
Accepted date: 28 June 2021

Please cite this article as: Priyanka Agrawal , Arjen Mascini , Tom Bultreys , Hamed Aslannejad , Mariëtte Wolthers , Veerle Cnudde , Ian B. Butler , Amir Raoof , The impact of pore-throat shape evolution during dissolution on carbonate rock permeability: pore network modelling and experiments, *Advances in Water Resources* (2021), doi: https://doi.org/10.1016/j.advwatres.2021.103991

The impact of pore-throat shape evolution during dissolution on carbonate rock permeability: pore network modelling and experiments

Priyanka Agrawal[1], Arjen Mascini[2], Tom Bultreys[2], Hamed Aslannejad[1], Mariëtte Wolthers[1], Veerle Cnudde[1,2], Ian B. Butler[3] and Amir Raoof*[1]

[1]Department of Earth Sciences, Utrecht University, Utrecht, Netherlands,

[2]PProGRess/UGCT, Department of Geology, Ghent University, Ghent, Belgium

[3]School of Geosciences, University of Edinburgh, Edinburgh

* Corresponding Author: a.raoof@uu.nl

Highlights

- Calcite dissolution can generate a spectrum of pore shape geometries.
- In existing PNMs, conductance relations ignore pore shape evolution.
- New conductance relations were derived from single pore scale simulations.
- These relations are a function of volume and imposed dissolution regime.
- Permeability may be overestimated by up to 27% if pore shape change is neglected.

ABSTRACT

Pore network model simulation (PNM) is an important method to simulate reactive transport processes in porous media and to investigate constitutive relationships between permeability and porosity that can be implemented in continuum-scale reactive-transport modelling. The existing reactive transport pore network models (rtPNMs) assume that the initially cylindrical pore throats maintain their shape and pore throat conductance is updated using a form of Hagen-Poiseuille relation. However, in the context of calcite dissolution, earlier studies have shown that during dissolution, pore throats can attain a spectrum of shapes, depending upon the imposed reactive-flow conditions (Agrawal et al., 2020). In the current study, we derived

new constitutive relations for the calculation of conductance as a function of pore throat volume and shape evolution for a range of imposed flow and reaction conditions. These relations are used to build and improved new reactive pore network model (nrtPNM). Using the new model, the porosity-permeability changes were simulated and compared against the existing pore network models.

In order to validate the reactive transport pore network model, we conducted two sets of flow-through experiments on two Ketton limestone samples. Acidic solutions (pH 3.0) were injected at two Darcy velocities i.e., 7.3×10^{-4} and 1.5×10^{-4} $m.s^{-1}$ while performing X-ray micro-CT scanning. Experimental values of the changes in sample permeability were estimated in two independent ways: through PNM flow simulation and through Direct Numerical Simulation. Both approaches used images of the samples from the beginning and the end of experiments. Extracted pore networks, obtained from the micro-CT images of the sample from the beginning of the experiment, were used for reactive transport PNMs (rtPNM and nrtPNM).

We observed that for the experimental conditions, most of the pore throats maintained the initially prescribed cylindrical shape such that both rtPNM and nrtPNM showed a similar evolution of porosity and permeability. This was found to be in reasonable agreement with the observed porosity and permeability changes observed in the experiment. Next, we have applied a range of flow and reaction regimes to compare permeability evolutions between rtPNM and nrtPNM. We found that for certain dissolution regimes, neglecting the evolution of the pore throat shape in the pore network can lead to an overestimation of up to 27% in the predicted permeability values and an overestimation of over 50% in the fitted exponent for the porosity-permeability relations. In summary, this study showed that while under high flow rate conditions the rtPNM model is accurate enough, it overestimates permeability under lower flow rates.

Keywords: Carbonate dissolution; Reactive transport; Micro-CT; pore network model; Porosity-permeability relation

1. INTRODUCTION

Numerous applications require an understanding of fluid interactions with porous solid phases. Examples include optimization of the recovery from hydrocarbon reservoirs and prediction of the long-term consequences of CO_2 injection in the subsurface. Calcite dissolution is an important reaction in the subsurface reservoirs. Several studies have demonstrated that during calcite dissolution, a multitude of physical and chemical processes operate at the pore scale which govern the evolution of the porous medium. Such modification of the porous medium and the related porosity-permeability relations is a function of the initial heterogeneity of the rock and of the dissolution conditions like the injection rate and chemistry of the injected fluid (e.g., Agrawal et al., 2020; Golfier et al., 2002; Hoefner and Fogler, 1988; Li et al., 2008; Luquot et al., 2014; Luquot and Gouze, 2009; Meile and Tuncay, 2006; Molins et al., 2014). One approach to comprehend the complexity of calcite dissolution process is through using pore-scale models such as pore network models (PNMs).

Several pore network formulations have been developed to present porous media topology and angular pore geometries (Acharya et al., 2005; Al-Gharbi and Blunt, 2005; Ghanbarian B., Hunt A. G., 2016; Raoof et al., 2013; Raoof and Hassanizadeh, 2012, 2009). Some studies have used pore throats with varying shapes, such as sinusoidal or other converging-diverging shapes (Acharya et al., 2005; Al-Gharbi and Blunt, 2005), for which analytical expressions can be applied to calculate pore conductance (Acharya et al., 2005; Ghanbarian B., Hunt A. G., 2016; Raoof and Hassanizadeh, 2012). Correct estimation of the hydraulic conductance values of the pores throats is required to obtain an accurate permeability for the sample.

In the context of calcite dissolution, the existing pore network models use a network of spherical pores bodies and cylindrical pore throats to simulate the related reactive transport

processes (Mehmani et al., 2012; Nogues et al., 2013; Raoof et al., 2012). These pore network models provide porosity-permeability relations as a function of the specific dissolution condition, which is a key input for continuum scale models. An important consideration in the existing pore network models is related to the way conductance of the pore throat is updated during the calcite dissolution.

Most pore network models assume that pore throats, having initially a uniform circular cross section along their length, preserve their form throughout dissolution, irrespective of the flow and reaction regimes. Consequently, in response to dissolution, pore conductance values can be calculated using the Hagen-Poiseuille relation. However, it has been shown that initially uniform pore throat structures can develop into a spectrum of pore throat shapes with circular cross sections of variable diameter along their length depending on the flow and reaction regimes (e.g., Agrawal et.al., 2020). For example, under diffusion and reaction dominated dissolution regimes, the pore throat structure changes into a half-hyperboloid (i.e., conical) shape. Under this condition, the Hagen-Poiseuille equation would result in an overestimation of pore throat conductance. Agrawal et al. (2020) showed that the conductance evolution in the pore network models should include information on pore throat shape evolution that takes the reaction regime into account. As mentioned earlier, some PNMs have been developed with originally non-uniform shapes of pore throats, however, no pore network-based study has incorporated the dissolution induced evolution of pore throat shapes.

In this study, we link the evolving shape of pore throats, under a wide range of conditions, to the resulting pore throat conductance values using reactive transport simulations. We implemented the correlation relations for the evolution of conductance as a function of pore throat shape and volume (Agrawal et.al., 2020) in a pore network extracted from experimental micro-CT data, to simulate reactive transport across the rock sample in a modified PNM. The outcome was compared to the Hagen-Poiseuille PNM approach and to the permeability

evolution determined experimentally using micro-CT. Finally, the impact of the new conductance evolution relationship on porosity-permeability relations was tested for a range of flow and reaction regimes.

2. EXPERIMENTAL METHOD

In this study, we used an oolitic limestone sample, Ketton Limestone, quarried from the Upper Lincolnshire Limestone Formation (village of Ketton in Rutland, England). Two plugs with a diameter of 6*mm* and an approximate length of 12*mm* were extracted from the homogeneous oolitic block. Hereafter, these samples are referred as K1 and K2. Two sets of reactive transport experiments were conducted on these samples. The injecting solution contained HCl acid with a pH value of 3.0 applied under two flow rates provided in Table 1. The environmental micro-CT (EMCT) scanner (Bultreys et al., 2016) at the Centre for X-ray Tomography (www.ugct.ugent.be) was used to image the progress of calcite dissolution with a reconstructed voxel size of 6μm. Each dynamic scan consisted of 2200 projections recorded in a total scan time of around 15 minutes. The sample was scanned at the beginning and at the end of the experiment. Data from raw projections were reconstructed into a 3D stack volume using the filtered back- projection method implemented in Octopus Software (Vlassenbroeck et al., 2007).

Table 1: Parameters applied in two micro-CT experiments

Experiment	Porosity	Flow rate ($m^3.s^{-1}$)	Darcy velocity ($m.s^{-1}$)	pH of injected solution	Injection duration (Minutes)
E1-HQ	0.18	2.05×10^{-8}	7.3×10^{-4}	3.0	102

E2-LQ	0.13	4.33×10^{-9}	1.5×10^{-4}	3.0	330

Next, 3D datasets were filtered using a non-local means filter and segmented with the watershed segmentation method (Avizo 9.5.0). Table 1 provides the porosity values computed from the segmented image volumes of the sample from the beginning of the experiments. We observed that the computed porosity values in this study fall within the range of earlier reported image-based segmentation porosity values for the Ketton rock (e.g., Table 3 in Menke et al., 2017). These values differ from the measured bulk porosity (e.g., Table 1 in Menke et al., 2017) indicating that image segmentation include some (unavoidable) deviations from the measured bulk porosity values. For both experiments, the size of the segmented 3D volume was 1318×1316×2494 voxels from which smaller sub-volumes were used in this study as discussed in Section 3.2.1.

3. NUMERICAL METHODS

We performed pore-scale modeling at three different levels: i) single pore scale (where we simulated reactive transport for a single evolving pore space under different conditions, cf Agrawal et al. 2020), ii) pore network scale (where rock dissolution is simulated using PNM), and iii) Direct Numerical Simulations (DNS) using 3D imaged pore structures (where detailed flow field is obtained by simulating incompressible flow in the rock images). The single pore-scale model provided insight on the evolution of the conductance of a pore throat for a range of physiochemical conditions and was previously validated against experimental microfluidic experiments (Agrawal et al., 2020). In the current work, we develop constitutive relationships for dissolution-induced conductance based on results from this systematic single pore model. The evolution of porosity and permeability observed in the pore network model was validated against a Direct Numerical Solution of flow across the sample. Next, for a range of flow and

reaction regimes, pore network models were run with and without the new improved conductance relationships and the permeability results of both models were compared. Table 2 summarizes key details of various simulations used in this study.

Table 2. Overview of the various simulations performed in this study. [1]following method of Aslannejad et al. (2018); [2]following method from Raoof et.al. (2012).

Model	Label	Program	Obtains
Single-pore simulation of reactive transport			
	COMSOL	COMSOL Multiphysics®	Relationship describing impact of pore shape evolution on conductance evolution
3D pore space simulation of flow only			
	DNS	OpenFOAM	Permeability change from experimental images[1]
	foPNM	PoreFlow	Permeability change from the pore network extracted from experimental images[2]
3D pore space simulation of reactive transport			
	rtPNM	PoreFlow	Simulation of porosity and permeability evolution[2]
	nrtPNM	PoreFlow	Determine impact of pore shape evolution on simulated permeability evolution

3.1 Single pore-scale model

Pore-scale reactive transport utilizing a single capillary geometry were simulated by solving the Stokes equations for fluid flow and advection-diffusion-reaction equations for reactive transport of aqueous species (COMSOL Multiphysics®). Readers are referred to Agrawal et

al. (2020) for details of the simulations and their validation against microscopic experiments of reactive transport in calcite crystals. The modeled range of boundary conditions (i.e., injection rate, composition of injecting solution, and pore throat geometry) correspond conditions relevant to injection of CO_2 or acidic solution into carbonate rocks. Details of the simulated flow regimes, reaction regimes and pore throat geometries are provided in Table S1.

To investigate the control of the reaction and flow regimes over the evolution of pore throat conductance, we calculated three dimensionless parameters including the Péclet number, the Damköhler number, and the Geometry Factor at the beginning of each simulation. The Péclet number (*Pe*) was defined as:

$$Pe = \frac{vr}{D} \quad (1)$$

where, v is the average velocity at the inlet boundary, r is the radius of the pore throat (m) and D is the diffusion coefficient i.e., 3.36×10^{-9} $m^2.s^{-1}$.

The Damköhler number (*Da*) was defined as:

$$Da = \frac{r\ k}{v\ C_{Calcite}} \quad (2)$$

where, $C_{Calcite}$ is the density of surface sites of calcite i.e., 0.8×10^{-5} $mol.m^{-2}$ and k ($mol.m^{-2}.s^{-1}$) is obtained based on the forward rate constant in the kinetic rate law for calcite dissolution (i.e., the reaction rate constant k_1 in Equation 11 in Section 3.3.2) and the activity of H^+ ions (i.e., aH^+ in Equation 11 in Section 3.3.2) in the injected solution.

The Geometry Factor, GF, was defined as:

$$GF = \frac{l}{r} \quad (3)$$

where, l is the length of the pore throat.

The conductance g ($m^5.N^{-1}.s^{-1}$) of the pore throat was calculated from the imposed volumetric flux, F ($m^3.s^{-1}$), and the pressure drop across the pore throat, ΔP_{sp} ($N.m^{-2}$), as:

$$F = g\Delta P_{sp} \tag{4}$$

In the case of a cylindrical pore throat geometry and laminar flow, Equation 4 is equivalent to the following definition of conductance, g:

$$g = \frac{\pi r^4}{8\mu l} \tag{5}$$

where, μ is the viscosity of water, 0.001 Pa s at about 25 °C.

Section 4.2 provides the modified relations for the calculation of the pore throat conductance for a range of flow and reaction regimes.

3.2 Pore Network Generation

3.2.1 Pore networks extracted from the digital rock volumes

A total of five pore network structures were generated from the micro-CT images of Ketton using the maximal ball algorithm (Raeini et al., 2017). Two subsets of size 700×700×700 voxels, K1S1 and K1S2, were obtained from the digital volumes of the sample K1 at two different times i.e., t = 0 and t = 102 minutes. Similar sized subsets, K2S1 and K2S2, were extracted from the digital volumes of the sample K2 at the two experiment times i.e., t = 0 and t = 330 minutes, respectively. These subsets were utilized for the purpose of validation of the pore network model such that networks K1S1 and K2S1 were the starting pore networks to perform reactive transport simulation. Note that the selected time duration for both experiments leads to injection of comparable pore volumes i.e., 2442 in experiment E1-HQ and 1996 in the experiment E2-LQ (Table 1).

Another subset of size 300×300×300 voxel, namely, K1S3, was extracted from the digital volume of the sample K1 at an experiment time step t = 0 minutes. This subset was utilized for the sensitivity study of the modified conductance model presented in Section 4.3.

The position of these subsets with reference to the full volumes of the Ketton sample is shown in Figures 1 and S1. Figure 2 shows the frequency distribution of properties of the extracted pore networks such as pore body radius, pore throat radius, pore throat length and coordination number. Table 3 provides the statistics of each extracted pore network.

Table 3: Statistics of all five pore networks extracted from the imaged rock samples. [1]Porosity of the extracted pore network; [2] Permeability from single phase flow simulation on the extracted pore networks.

	K1S1	K1S2	K2S1	K2S2	K1S3
Number of pore bodies	2088	1787	2015	1960	184
Number of pore throats	3794	3108	3324	3293	316
Mean coordination number	3.63	3.48	3.30	3.36	3.43
Mean pore body radius(m)	48.38×10^{-6}	53.55×10^{-6}	46.51×10^{-6}	48.67×10^{-6}	48.22×10^{-6}
Mean pore throat radius(m)	26.23×10^{-6}	31.22×10^{-6}	24.80×10^{-6}	26.52×10^{-6}	25.94×10^{-6}
Mean pore throat length(m)	112.41×10^{-6}	118.40×10^{-6}	107.29×10^{-6}	110.14×10^{-6}	117.78×10^{-6}
[1]Porosity	0.15	0.16	0.12	0.13	0.19

[2]Permeability (k_{foPNM}) (mD)	2809.6	6511.6	1226.1	2865.5	5515.6

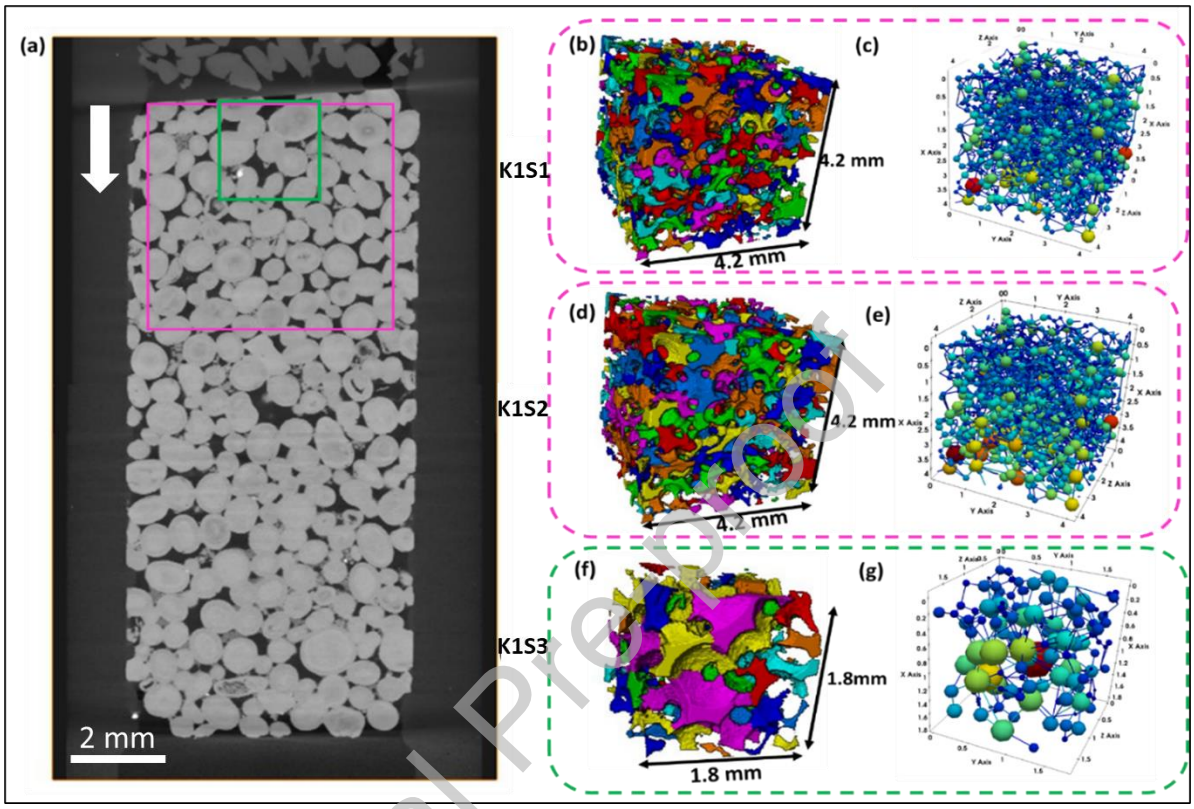

Figure 1: **pore structures and sample sub-volumes**. **(a)** a vertical slice obtained using the micro-CT volume of the sample K1 showing the position and sizes of the extracted sub-volumes K1S1 (t =0), K1S2 (t = 102 min) (magenta color lines) and K1S3 (t =0) (green color line). The white arrow shows the flow direction (image is rotated 180° compared to experimental position, where flow was upward). Panels (**b**), (**d**) and (**f**) indicate the digital subsets, K1S1, K1S2 and K1S3, respectively. Panels (**c**), (**e**) and (**g**) are the extracted pore networks from the corresponding sub-volumes.

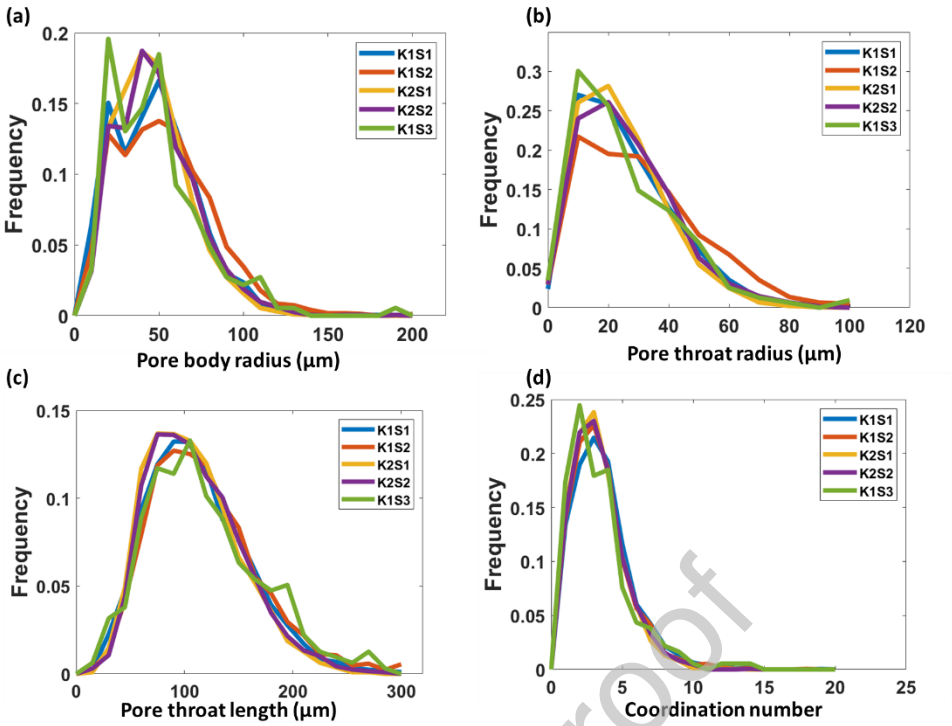

Figure 2: **sample pore sizes.** Pore size distribution for **(a)** pore body radius **(b)** pore throat radius, and **(c)** pore throat length. **(d)** the distribution of pore coordination numbers.

3.3 Pore Network Model

The pore network model utilized in this study is an adaptation of the previously developed pore-scale model by Raoof et al. (2012). In the following, this model is discussed briefly.

3.3.1 Flow and Solute transport

For this study, single phase flow was established across the pore network. This was achieved by assuming laminar flow along each pore throat of the network (i.e., Reynolds number is less than 1). Flux through a pore throat was described by the Hagen-Poiseuille equation as:

$$q_{ij} = g_{ij}(p_j - p_i) \quad (6)$$

where q_{ij} is total volumetric flux through the pore throat ij , g_{ij} is the conductance of the pore throat ij, and p_i and p_j are the pressures in pore bodies i and j, respectively. The simulated pore network models in this study utilized the Hagen-Poiseuille relation (i.e., Equation 5) and modified conductance relations (i.e., Equations 18) for calculation of the pore throat conductance.

For incompressible, saturated flow conditions, the sum of fluxes of all pore throats connected to a pore body was equated to zero. This implies that the amount of flux going to a pore body should be equal to the amount of flux coming out of that pore body:

$$\sum_{j=1}^{N_k} q_{ij} = 0;\ j = 1,2, \dots N_k \tag{7}$$

where N_k is the coordination number of pore body k.

Equation 7 is valid for all pore bodies of the network except those present at the inlet and outlet face of the network. Combination of Equations 6 and 7 resulted in a linear system of equations to be solved for the pressure of the pore bodies and the volumetric flux through the pore throats. We have used a constant Darcy velocity boundary condition at the inlet face, a constant pressure (i.e., atmospheric pressure) boundary condition at the outlet face, and no-slip boundary conditions was applied at the lateral faces of the network.

From the imposed Darcy velocity (u_D) and pressure difference between the inlet and outlet faces (ΔP_{PNM}), the absolute permeability of the pore network is calculated from:

$$k_{PNM} = \frac{\mu\, u_D\, L}{\Delta P_{PNM}} \tag{8}$$

where, L is the length of the pore network along the flow direction.

All the chemical components are transported through the pore network by advection and diffusion processes. For a given pore body i and for the flow conditions under which fluid flowing from pore body j towards pore body i, through pore throat ij, we can define the transport of the k^{th} chemical component as:

$$V_i \frac{d}{dt}(c_{k,i}) = \sum_{j=1}^{N_{in}^{throat}} q_{ij} c_{k,ij} - Q_i c_{k,i} + \sum_{j=1}^{z_i} D A_{ij} \frac{(c_{k,ij} - c_{k,i})}{l_{ij}} - R_{k,i} \quad (9)$$

where, V_i , Q_i and $c_{k,i}$ are the volume, volumetric flow rate and concentration of k^{th} component in pore body i, respectively. The left-hand side (L.H.S) of the Equation 9 provides the rate of change of concentration for the k^{th} component in the pore body i over time. This rate is a combined output of the advective, diffusive and reactive rates. The first term on the right-hand side (R.H.S) of the Equation 9 calculates the total amount of the incoming flux of each component through N_{in}^{throat} upstream pore throats (i.e., pore throats flowing into pore body *i*). This calculation utilizes the volumetric flow rate (q_{ij}) and concentration ($c_{k,ij}$) in pore throat ij. The second term on the R.H.S calculates the total outflux of the k^{th} component. The third term on the R.H.S calculates the diffusion rate of the k^{th} component through z_i connected pore throats. This calculation utilizes the molecular diffusion coefficient (D) and the cross-sectional area of the throat (A_{ij}). The last R.H.S term, $R_{k,i}$, defines changes due to chemical reactions of the k^{th} component taking place inside the pore body.

Similarly, the mass balance equation for pore throat ij and for the case when the fluid is flowing from pore body j to pore throat ij, can be written as:

$$V_{ij} \frac{d}{dt}(c_{k,ij}) = q_{ij} c_{k,j} - q_{ij} c_{ij} + D\, A_{ij} \frac{(c_{k,j} - c_{k,ij})}{l_{ij}} + D\, A_{ij} \frac{(c_{k,i} - c_{k,ij})}{l_{ij}} - R_{k,ij} \quad (10)$$

where V_{ij} , q_{ij} and $c_{k,ij}$ are the volume, volumetric flow rate and concentration of k^{th} component in pore throat ij, respectively. $R_{k,ij}$ provides feedback from reactions of the k^{th} component taking place inside the pore throat.

3.3.2 Reactions and rate laws

To describe the calcite dissolution system, we have incorporated a total of four reactions. Out of those four reactions, three reactions involving only aqueous species are described using equilibrium relationships, whereas the dissolution of calcite is described by a kinetic rate law. Details of equilibrium reactions are provided in Table 4.

Plummer (1978) has identified three main mechanisms through which calcite dissolution takes place. Accordingly, we have defined the calcite dissolution rate as:

$$Rate = A\,(k_1 a_{H^+} + k_2 a_{H_2CO_3^*} + k_3)\left(1 - \frac{a_{Ca^{2+}}\, a_{CO_3{}^{2-}}}{K_{eq}}\right) \tag{11}$$

where, A is the reactive surface area of calcite and a_i is the activity of species i. k_1 = 8.64 × 10^{-5} ($m.s^{-1}$), k_2 = 4.78×10^{-7} ($m.s^{-1}$) and k_3 = 2.34×10^{-9} ($m.s^{-1}$) are reaction rate constants at 25°C (Plummer and Busenberg, 1982). K_{eq} = $10^{-8.48}$ is the equilibrium constant for calcite dissolution (Plummer and Busenberg, 1982).

Table 4: Equilibrium rate laws of CO_2-H_2O system and respective equilibrium constants

Reactions	Equilibrium rate constant from Plummer and Busenberg, 1982
$CO_2(aq) = H^+ + HCO_3^-$	[a]4.5×10^{-7}
$HCO_3^- = H^+ + CO_3^{2-}$	[a]4.78×10^{-11}

$H_2O = H^+ + OH^-$	1×10^{-14}

3.3.3 Modeling parameters

We have utilized two sets of flow and chemical conditions for pore network modeling. The first set is derived from the experimental parameters (Table 1) and the second set covers the range of reaction and flow regimes which are relevant to acid stimulation experiments in carbonate reservoirs.

In the experiments, we injected the solutions at a fixed flow rate. Table 5 provides the magnitude of the calculated Darcy velocity for the experiments E1-HQ and E2-LQ. Models corresponding to these experiments utilized the respective value of the Darcy velocity for injecting a solution with the pH value of 3.0. Additional sets of utilized Darcy velocities and pH of the injected solutions are provided in Table 5. Lower pH values of the injected acid are relevant to acid stimulation applications in carbonate reservoirs (Al-Ameri and Gamadi, 2020; Janbumrung and Trisarn, 2017; Leong and Ben Mahmud, 2019). The composition of these solutions was calculated using PhreeqC (Parkhurst and Appelo, 2013) and phreeqc.dat database (Table S2).

Table 5: Statistics related to the simulated pore networks

Sample	Experiment	Darcy Velocity ($m.s^{-1}$)	pH of injecting solution	Simulation Duration (Minutes)	Injected Pore Volumes	$\widetilde{Pe}$	$\widetilde{Da_I}$	$\widetilde{Da_{II}}$
K1S1	E1-HQ	7.3×10^{-4}	3.0	35.5	2442	974	5.82×10^{4}	5.98×10^{1}
K2S1	E2-LQ	1.5×10^{-4}	3.0	115	1996	192	5.82×10^{4}	3.03×10^{2}
K1S3		1.5×10^{-4}	1.0	100	56	1.70	1.04×10^{6}	6.13×10^{5}
K1S3		8.3×10^{-5}	1.0	20	56	8.50	1.04×10^{6}	1.23×10^{5}

K1S3	15×10^{-4}	1.0	10	56	17.00	1.04×10^{6}	6.13×10^{4}
K1S3	30×10^{-4}	1.0	5	56	34.00	1.04×10^{6}	3.07×10^{4}
K1S3	75×10^{-4}	1.0	2	56	85.00	1.04×10^{6}	1.23×10^{4}
K1S3	1.5×10^{-4}	3.0	3000	1670	1.70	1.07×10^{4}	6.30×10^{3}
K1S3	8.3×10^{-5}	3.0	600	1670	8.50	1.07×10^{4}	1.26×10^{3}
K1S3	15×10^{-4}	3.0	300	1670	17.00	1.07×10^{4}	6.30×10^{2}
K1S3	30×10^{-4}	3.0	150	1670	34.00	1.07×10^{4}	3.15×10^{2}
K1S3	75×10^{-4}	3.0	60	1670	85.00	1.07×10^{4}	1.26×10^{2}
K1S3	1.5×10^{-4}	5.0	3000	1670	1.70	3.87×10^{2}	2.28×10^{2}
K1S3	8.3×10^{-5}	5.0	600	1670	8.50	3.87×10^{2}	4.56×10^{1}
K1S3	15×10^{-4}	5.0	300	1670	17.00	3.87×10^{2}	2.28×10^{1}
K1S3	30×10^{-4}	5.0	150	1670	34.00	3.87×10^{2}	1.14×10^{1}
K1S3	75×10^{-4}	5.0	60	1670	85.00	3.87×10^{2}	4.56

In order to categorize the simulated flow and reaction regimes, we have defined the macroscopic Peclet number ($\widetilde{Pe}$) and Damköhler numbers ($\widetilde{Da_I}$ and $\widetilde{Da_{II}}$) as:

$$\widetilde{Pe} = \frac{u_D\, L}{D} \tag{12}$$

$$\widetilde{Da_I} = \frac{L^2\, k_1\, a_{H^+}}{D\, C_{Calcite}} \tag{13}$$

$$\widetilde{Da_{II}} = \frac{L\, k_1\, a_{H^+}}{U_D\, C_{Calcite}} \tag{14}$$

where, u_D is the Darcy velocity (m.s^{-1}) and L is the length of the pore network along the flow direction. Table 5 provides $\widetilde{Pe}$, $\widetilde{Da_I}$ and $\widetilde{Da_{II}}$ numbers for all the simulated models.

Note that the Pe and Da numbers without ~sign were defined at the scale of an individual throat while Pe and Da numbers with ~sign were defined at the scale of pore network.

3.4 Direct flow simulation of pore-scale images

In order to compare the permeability values obtained from PNM results, we have performed pore-scale flow DNS. We have used the Volume of Fluid (VOF) method implemented in OpenFOAM Computational Fluid Dynamic (CFD) package to solve incompressible flow using a semi-implicit method for pressure (Aslannejad et al., 2018; Bedram and Moosavi, 2011).

Numerical three-dimensional simulation of incompressible linear-viscous flow was done by solving the Navier-Stokes equations:

$$\rho\left(\frac{\partial u}{\partial t} + u.\nabla u\right) = -\nabla p + \mu\nabla^2 u \tag{15}$$

$$\nabla.u = 0 \tag{16}$$

where, p is pressure, u is velocity, μ is the viscosity of water (μ = 0.001 Pa.s) and ρ is the density of water (ρ = 1000 kg.m^{-3}).

The flow equations are solved by applying a constant pressure difference between the inlet and the outlet faces (ΔP_I) and a no-slip boundary condition at the remaining faces. This yielded the velocity and pressure for each voxel in the domain. The flow rate, Q (m^3.s^{-1}) was calculated as $Q = \int u_x A_x$, where A_x (m^2) is the cross-sectional area of the inlet face perpendicular to the direction of flow x and u_x is the inlet face velocity component in the direction of flow. From the flow rate (Q) and the imposed pressure difference (ΔP_{DNS}), absolute permeability of the 3D XMT image, k_{DNS} (m^2) is calculated using Darcy equation:

$$k_{DNS} = \frac{\mu\, Q\, L_x}{\Delta P_{DNS}\, L_y\, L_z} \tag{17}$$

where, L_x, L_y and L_z are the domain lengths in each direction.

4. RESULTS AND DISCUSSIONS

Section 4.1 presents a comparison of the pore network models against the observations from micro-CT experiments. Next, using single-pore simulations, we derived correlation relations for the conductance of pore throats in Section 4.2. These relations were implemented in the new PNM (nrtPNM). Section 4.3 provides comparison of permeability evolution from nrtPNM versus rtPNM for the experimental conditions. Section 4.4 extends this comparison for a range of transport and reaction regimes. In Section 4.5 we present the impact of flow and reaction conditions over the porosity-permeability relations obtained from nrtPNM *versus* rtPNM.

4.1 Validation of the reactive transport pore network model (rtPNM) with the micro-CT experiments

Two rock pore networks i.e., K1S1 and K2S1 were simulated with similar initial and boundary conditions to the experiments E1-HQ and E2-LQ, respectively. At time t =0, samples were filled with a fluid solution equilibrated with calcite. In the experiment E1-HQ, injection of a solution with a pH value of 3.0 initiated calcite dissolution which shows itself as a decreasing amount of calcite in Figure 3e. Figure 3a-d shows the corresponding time-based evolution of the average chemical species concentrations. The pH of the solution inside the sample decreased continuously as a larger number of pores were penetrated by the acidic solution (Figure 3a-d). The acid arrival time for each pore throat depends on its distance from the inlet boundary and its connectivity with the dominant flow channels. The inlet area of the sample reaches a steady state in shorter time compared to the outlet area (Figure S2). Moreover, the steady state pH of the inlet area is lower than that of the outlet area (Figure S2). This indicates that within the simulation time, a significant number of pore throats located in the outlet area were not yet filled with the inflow solution chemistry. From the distribution of pH of the solution inside the sample, after injection of around 2442 pore volumes, we observed that more

than 40% of pore throats were filled with the inflow solution pH value of 3.0, while ~ 1% pore throats retained their calcite equilibrated solution (Figure S3a). Compared to experiment E1-HQ, the lower injection rate in experiment E2-LQ further delayed the attainment of steady state for different part of the sample (Figure S4). Consequently, after around 1996 pore volumes of acid injection in the experiment E2-LQ, a significant fraction of pore throats was filled with solutions having pH values larger than 7 (Figure S3b).

Figure 4 compares the evolution of porosity and permeability in the reactive transport model (rtPNM) against the experimental porosity and permeability data, obtained from the time-lapse micro-CT images. Experimental data of changes in porosity were calculated from the porosities of the extracted pore networks that were derived from the digital images of the sample belonging to the start and end of the experiment (Table 3). The model showed a smaller amount of dissolved calcite compared to the measured experimental values (Figure 4a). A possible cause could be the deviation of the implemented rates in models from those operating in the experiments. Such deviation can cause, for example, slower penetration rate of the acid in the simulations compared to the experiment. For the model related to the experiment E1-HQ, 2442 pore volumes of acid injection were not sufficient to attain a complete steady state pH in the system (Figure 3e).

For both experiments, we observed a fairly good agreement between the permeability evolution in the reactive transport model (k_{rtPNM}) and in the dissolution experiments (k_{foPNM} and k_{DNS}) (Figure 4b). Additionally, we observed that for the experiment E2-LQ, k_{foPNM} agrees well with k_{DNS}, while for the experiment E1-HQ, the two values differ significantly (Figure 4b). The difference between permeabilities obtained through foPNM and DNS is likely due to the simplification of the pore-scale geometrical features during extraction of pore network (Boever et al., 2016).

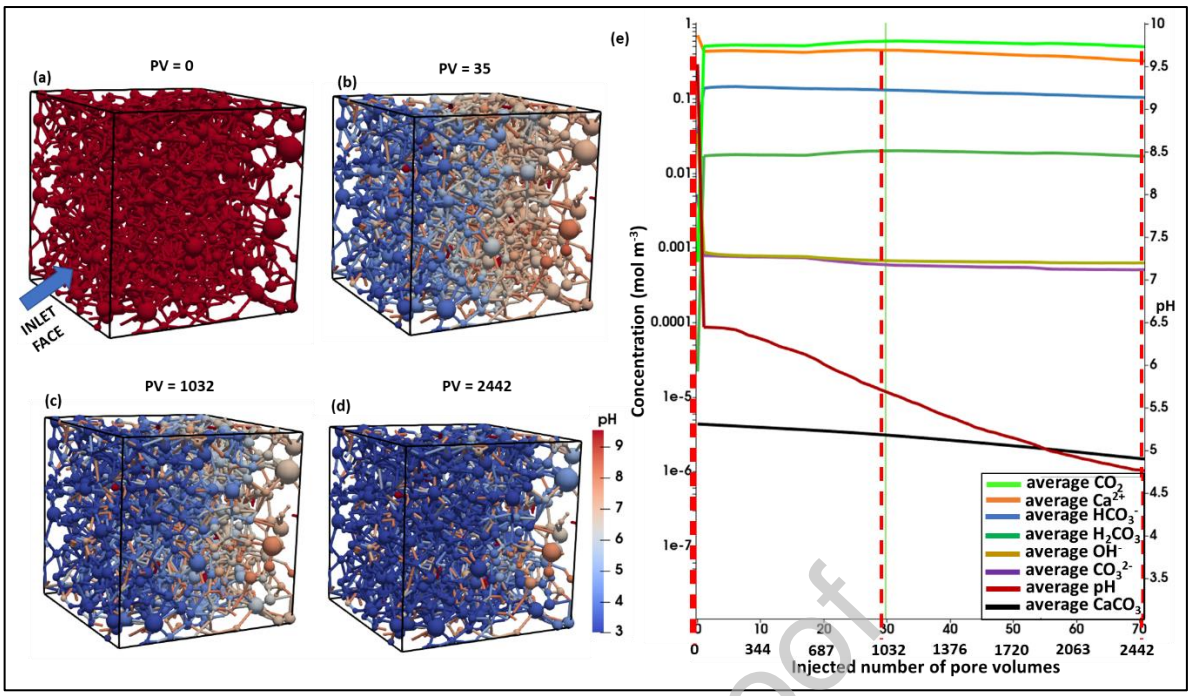

Figure 3: **concentration fields. (a-d)** show 3D distribution of pH within the reactive transport pore network model (rtPNM) corresponding to the experiment E1-HQ at times corresponding to pore volumes of **(a)** 0, **(b)** 35, **(c)** 1032, and **(d)** 2442. **(e)** evolution of the concentration of aqueous species with the injected number of pore volumes. Note: to obtain the 1D time plot, the 3D concentration fields are averaged within the entire sample at different times.

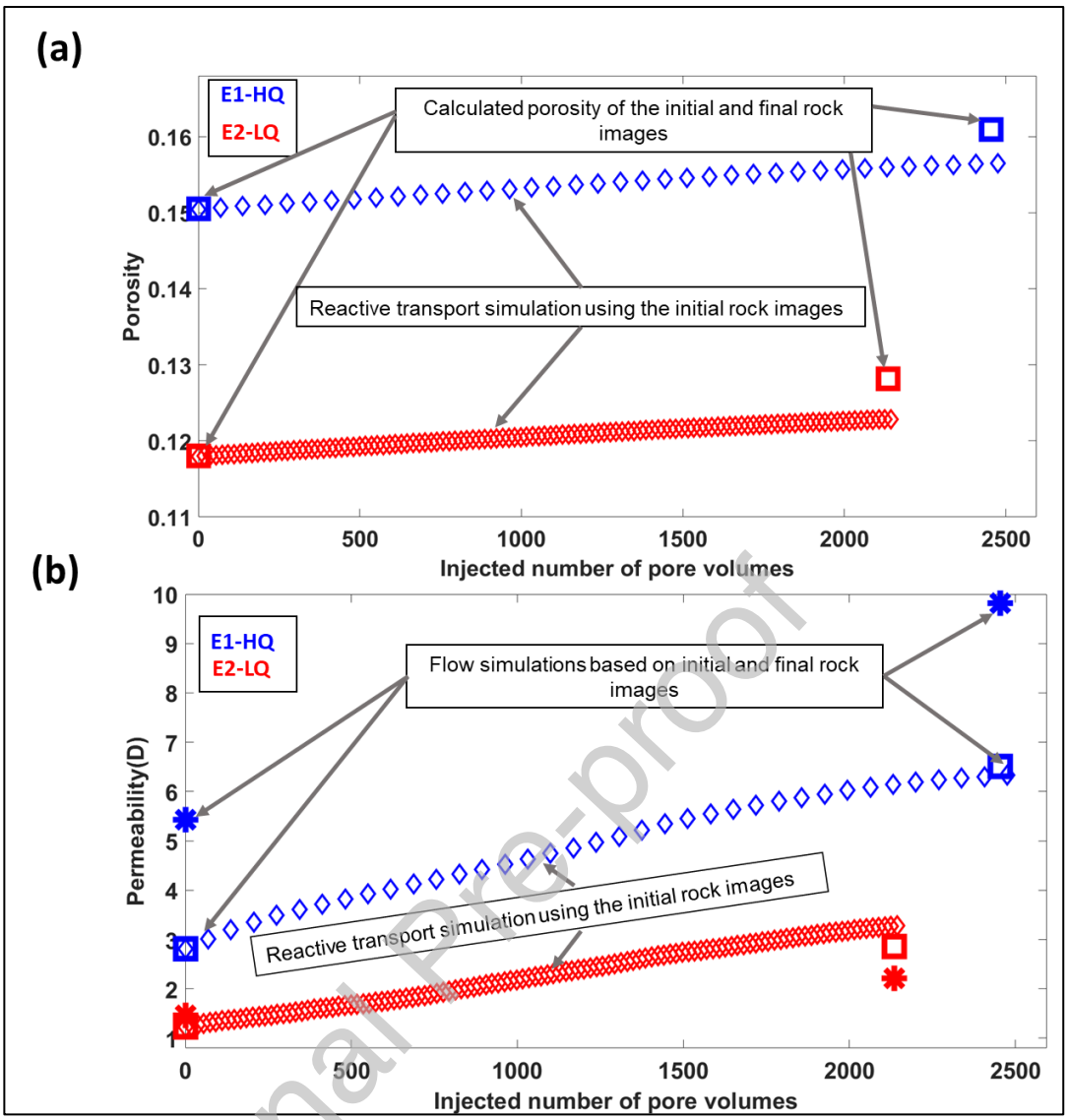

Figure 4: (a) Porosity evolution and **(b)** permeability evolution against the injected pore volumes for experiments E1-HQ (high flow rate) and E2-LQ (low flow rate). Diamond markers correspond to rtPNM which use the initial sample pore structure as their initial condition and perform reactive transport to calculate and predict evolution of samples over time. Asterisks and squares in panel (b) show results of flow only simulations performed on the 3D image of the sample from the beginning and end of the experiments: asterisks show results from DNS and squares show results from foPNM simulations.

4.2 Derivation of the constitutive relations for calculation of pore throat conductance

Agrawal et.al. (2020) have shown that the imposed flow and reaction regimes determine the evolution of the pore throat shape and subsequent evolution of conductance during calcite dissolution. Figures 5 and S5 present the dependency of the conductance of a pore throat on the volume of that pore throat for the simulated flow and reaction regimes while the length and initial radius of the pore throat are fixed at a value of 500×10^{-6} and 40×10^{-6} m, respectively.

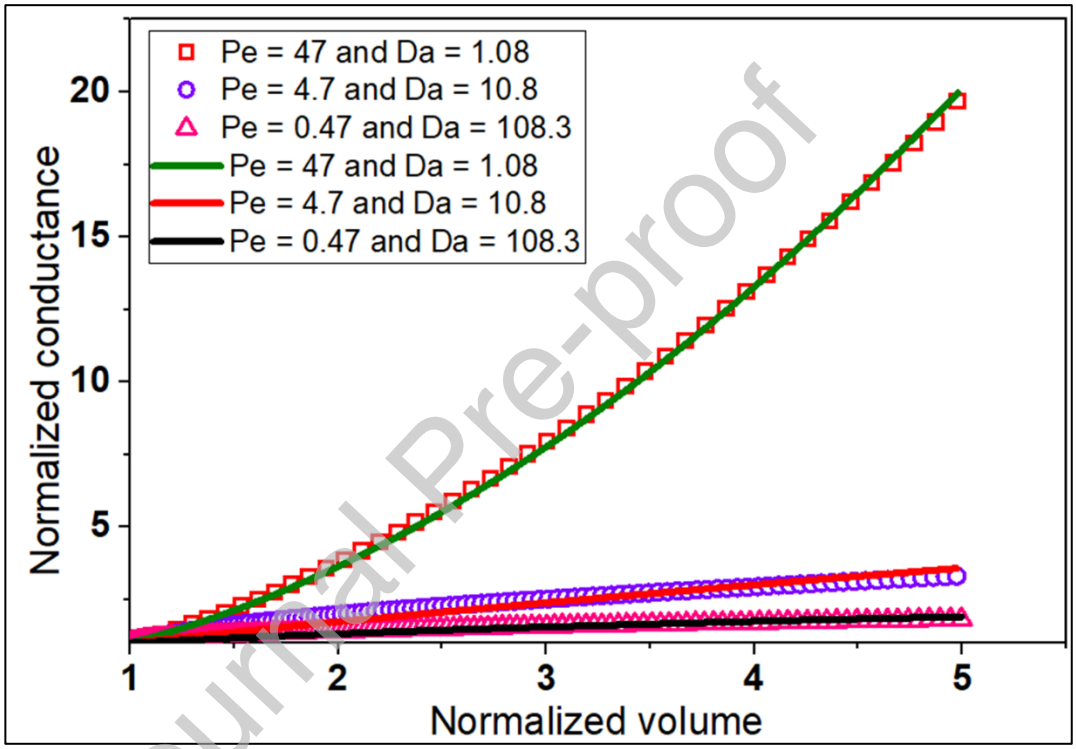

Figure 5: pore conductance relations. Normalized values of pore throat conductance as a function of normalized volume of pore throat for some of the simulated flow and reaction regimes (pore throat length and initial radius are fixed at 500.0×10^{-6} m and 40.0×10^{-6} m, respectively). For each dataset, markers represent the data points and the solid lines represent the fitted curves (Equation 18).

We observe that, at any time during calcite dissolution, the updated pore conductance can be related to the modified volume of the pore throat using an exponent, *b*:

$$\frac{g_t}{g_o} = \left(\frac{V_t}{V_o}\right)^b \tag{18}$$

where g_t and g_o are the conductance of the pore throat, calculated from Equation 4, g_o at time t=0s and g_t at time t during the course of the dissolution; similarly, V_t and V_o are the volume of pore throat at time t=0s and at time t. Exponent *b* represents the distinctiveness and topology of the evolved pore shape. Since the evolution of the pore throat shape is guided by a number of parameters such as initial geometry of the pore throat and imposed flow and reaction regimes, *b* is a function of these parameters (Figure 6a).

Figure 6a shows that under advection dominated regimes, indicated by *Pe*>1, and reaction-controlled regimes, indicated by *Da*<1, the *b* coefficient approaches a value of 2.0. Under these regimes, the shape of the pore throat remains cylindrical throughout the dissolution period (Agrawal et al., 2020: Figure 7b). Under this condition (i.e., *b*=2.0), our relation (Equation 19) becomes equal to the Hagen Poiseuille relation (Equation 5). For diffusion dominated regimes, when *Pe*<1, and reaction dominated regimes, when *Da*>1, the cylindrical shape evolves into half-hyperboloid shapes (Agrawal et al., 2020: Figure 7a). For these cases, the value of *b* becomes smaller than 2.0 and the accurate pore conductance can be calculated from Equation 19. It should be noted that here, shape evolution implies that the profile of the shape along the flow path changes from cylinder to half-hyperboloid longitudinal while cross-section of the pore throat, i.e., perpendicular to the flow path, remains circular.

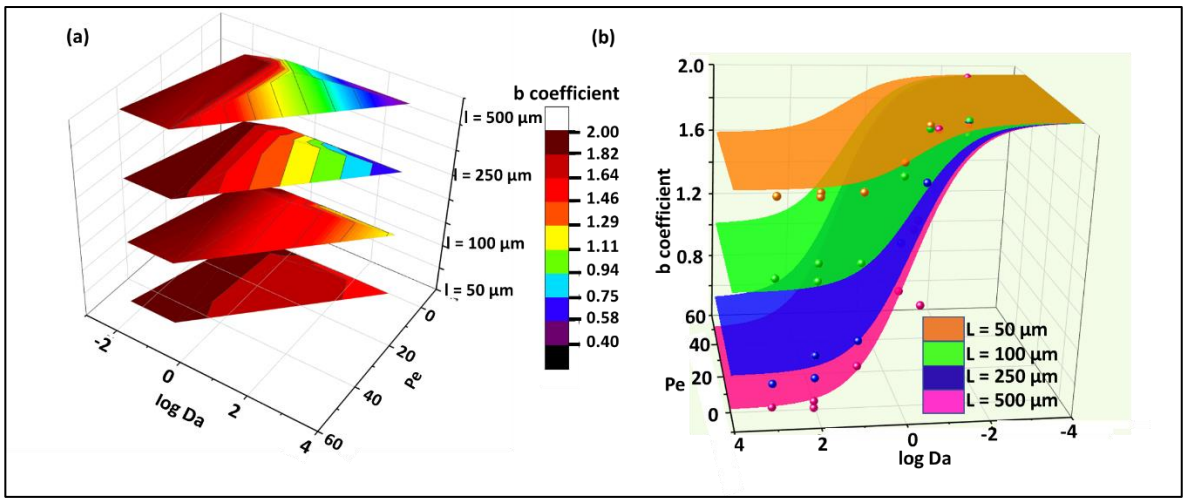

Figure 6: pore conductance parameters. (a) Dependency of the *b* coefficient (shown using the color legend) on the strength of reaction and flow regime (the horizontal axes) and pore throat lengths (shown as segregated colors. i.e., each surface corresponds to a certain pore throat length). Higher values of *b* coefficient correspond to higher *Pe* numbers and lower *Da* numbers. Pore throat length of value of 500.0×10^{-6} m shows a higher range for the *b* coefficient compared to a smaller pore throat length with a value of 250.0×10^{-6} m. **(b)** the fitted curved surface together with the data points used to obtain the best fit (SI Section S1; Table S1).

The relation for coefficient *b* can be expressed as:

$$b = A_1 + \frac{2 - A_1}{1 + \frac{Da^{p_3}}{Pe^{p_4}}} \tag{19}$$

$$A_1 = p_1 GF^{-p_2} \tag{20}$$

Values of fitting parameters (p_1, p_2, p_3 and p_4) were obtained using nonlinear least squares method (SI Section S1, Figure S6a). We have obtained a R-square value of 0.94 indicating that the fitted relationship and its parameters are able to describe data points (Figure S6b). Figure 6b shows the 3D plot of the fitted relation and the corresponding data points. In general, for reaction regimes corresponding to *Da*> 1 and *Da*<1, the fitted relationship captures the dependency of *b* over *Pe* number, *Da* number and *GF* (Figure 6b). Figure S7 shows the

sensitivity of the derived model over the testing data set. For most of the test data points, the % difference in the value of b calculated from the fitted model vs that obtained from numerical simulation is within 10% (Figure S7b). This assures the predictive capacity of the proposed model.

Next, along with Hagen Poiseuille's relation, we have used our developed relation to perform pore network model simulations. Hereafter, these two pore network models will be referred as rtPNM and nrtPNM (i.e., new model). In nrtPNM, at each time step of the simulation, using the updated *Pe* number, *Da* number, and *GF*, the *b* value was calculated for each pore throat of the pore network. Subsequently, for each pore throat of the pore network, the modification in conductance was calculated. In Sections 4.3 and 4.4, we compare the impact of these two pore network modeling approaches on the evolution of the permeability of the sample.

4.3 nrtPNM under flow and reaction regimes of micro-CT experiments

For the experiment E1-HQ, diffusion dominated pore throats are highlighted in red in Figure S8a after injection of around 2442 pore volumes. These pore throats either have $Pe<0.0001$ (i.e., diffusion is the major transport mechanism) or $0.0001<Pe<1$ (i.e., both diffusion and low velocity convection are controlling the transport). Part of the diffusion dominated pore throats, mostly pore throats with $Pe<0.0001$, have a *Da* number greater than 1 (highlighted in green color in Figure S8b). These pore throats will transform into non-uniform pore shapes, and a value of *b* smaller than 2.0 is obtained for the calculation of conductance using Equation 19 (highlighted in yellow color in Figure S8c). In the experiment E1-HQ, the fraction of such diffusion dominated, and reaction dominated pore throats is ~8%, whereas in the experiment E2-LQ, this fraction is ~11% (Figure S8d-S8f).

We observed that both rtPNM and nrtPNM provide porosity and permeability evolutions that are so similar that the results would overlap in Figure S9. This is because the flow conditions

for both experiments, which were selected to trigger visible porosity changes within the time frame of the micro-CT experiments, lead predominantly to advection dominated regimes as indicated by large $\widetilde{Pe}$ numbers (Table 5). Therefore, under these flow conditions, 89-92% pore throats keep their cylindrical shape during dissolution and nrtPNM agrees equally well as rtPNM with the experimentally determined porosities and permeabilities.

4.4 nrtPNM under different flow and reaction regimes

This section explores the influence of the injection velocity and pH value of the injected solution over the calcite dissolution processes and subsequent evolution of the petrophysical properties of the sample. Calcite dissolution is a combination of three processes: i) transport of the reactants towards the calcite surface, ii) interaction of reactants with the calcite surface and iii) removal of the products away from the calcite surface. The fluid velocity inside the pore throat determines the transport rate for the first and the last steps. The pH of the solution controls the rate of the second step. Calcite dissolution increases when a solution with a lower pH value is injected or the injection rates are increased. Figure 7 shows the impact of changing the injection rate, resulting in a different $\widetilde{Pe}$ number, on the evolution of porosity while the pH of the injected solution is fixed at a value of 1.0. For the injection of the same number of pore volumes, lowering of the acid injection rates leads to dissolution of a higher amount of calcite (Figure 7) as it increases the residence time of acid within the sample. We observed that the reactive transport conditions inside the pore network evolved constantly during dissolution (Figure S10). These updated reactive transport conditions of the pore throat were utilized in the calculation of new conductance value using Equation 19 and 20. Comparing results from nrtPNM and rtPNM, we observed similarity in the porosity evolution but difference in the permeability evolution (Figure 7). Figure S11 and S12 provide the evolution of porosity and permeability for remaining simulated cases.

Differences in the evolution of permeability in these models are proportional to the number of pore throats transforming into non-uniform shapes during dissolution. As mentioned earlier, these sets of pore throats belong to a diffusion dominated transport regime and a reaction dominated dissolution regime. For each of the simulated boundary conditions, we have identified the fraction of pore throats which fulfils this criterion (Table S3, Figure S13). For example, for a simulated network S5, injection of a solution with pH of 1.0 and a Darcy velocity of 3.17×10^{-6} m.s^{-1} results into development of a non-uniform shape for around 60% of pore throats (Figure 7: $\widetilde{Pe}$ = 1.70 and $\widetilde{Da_{II}}$ = 6.13×10^{5}). Consequently, for this case, we observed that rtPNM overestimates the permeability by around 27% as compared to nrtPNM. For all simulated boundary conditions, Figure 8 summarizes the percentage difference in the predicted value of permeability from these two models. This shows that for flow and reaction regimes corresponding to $\widetilde{Da_{II}}$ greater than 100 the two pore network models start to deviate and for $\widetilde{Da_{II}}$ greater than 10^{3} significant differences evolve the permeability prediction of the sample.

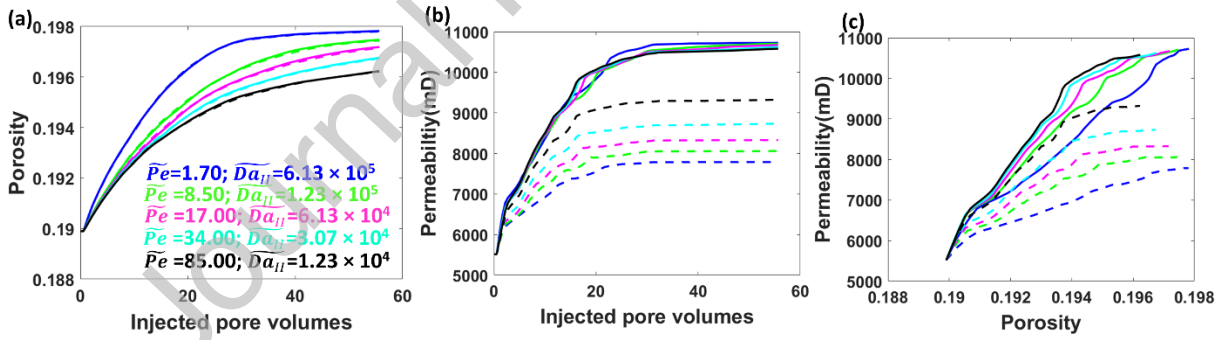

Figure 7: Evolution of porosity and permeability. (a) Porosity vs injected pore volumes **(b)** Permeability vs injected pore volumes and **(c)** Permeability vs Porosity, from rtPNM (solid lines) and nrtPNM (dotted lines). The inflow solution had a pH value of 1.0 and was injected using five different Darcy velocities. Note that the legend provided in panel **(a)**, is color coordinated with the plotted line colors and applicable for panels **(b)** and **(c)**, as well.

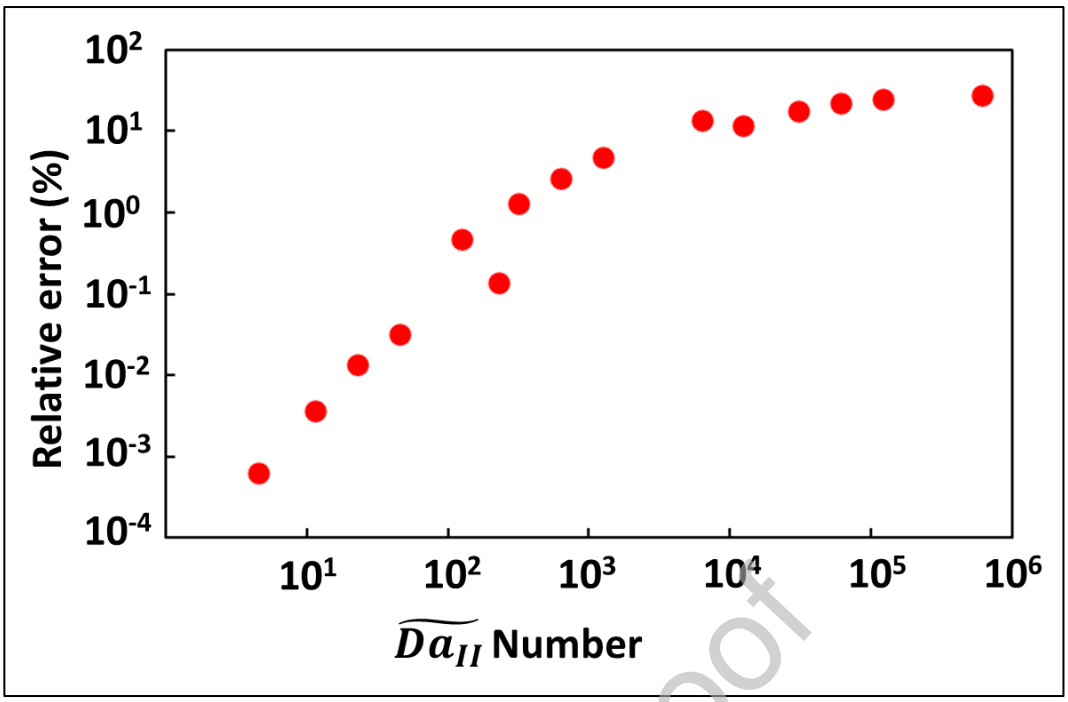

Figure 8: the obtained simulation accuracy. Relative percentage difference in the final permeability value of the sample simulated using the new conductance relation, nrtPNM, and the Hagen Poiseuille relation, rtPNM, under different $\widetilde{Da_{II}}$ numbers.

4.5 Implications for porosity-permeability relationship used at the field scale

Many continuum-scale models use a power law relation to determine the evolution of permeability from the changes in porosity (e.g., Hommel et al., 2018):

$$k_t = k_o \left(\frac{\emptyset_t}{\emptyset_o}\right)^{\alpha} \tag{21}$$

where k_o and $\emptyset_o$ are the initial permeability and porosity of a sample. The fitting parameter, α, depends on the initial properties of the rock and on the processes controlling the changes in the pore geometry (e.g., Parvan et al., 2020). The α value can either be obtained through theoretical derivation or through fitting of experiments and models. In this study, we observed that for a very similar rock sample, α is a function of the injection parameters such as Darcy velocity and acidity of the injected solution (Figure 9) (see also Nogues et al., 2013). Moreover,

we observed a temporal variation in α which indicates different phases of dissolution (Figure 9).

Figure 9 shows α as a function of the porosity of our samples for a set of simulations. First, for some of the injection conditions, rtPNM provided larger α values, by a factor of over 50%, as compared to the nrtPNM (Figure 9: $\widetilde{Pe}$=1.70 and $\widetilde{Da_{II}}$ = 6.13×10^5).

The initially large α value suggests that the first target of the acid reactions are the highly conductive paths where a small increment in the porosity results in large increment in permeability (Bernabé et al., 2003; Nogues et al., 2013). We observed that the increment in the injection velocity or in the pH of the injected solution leads to a consistent increase of α (Figure 9), irrespective of which model was used (rtPNM or nrtPNM). This can be explained by the fact that, in advection dominated regimes or in reaction-controlled regimes, the dissolution takes place more uniformly in the sample. Figure 9 again shows that at certain conditions, rtPNM is fine to be used, but at other conditions it will give an overestimation.

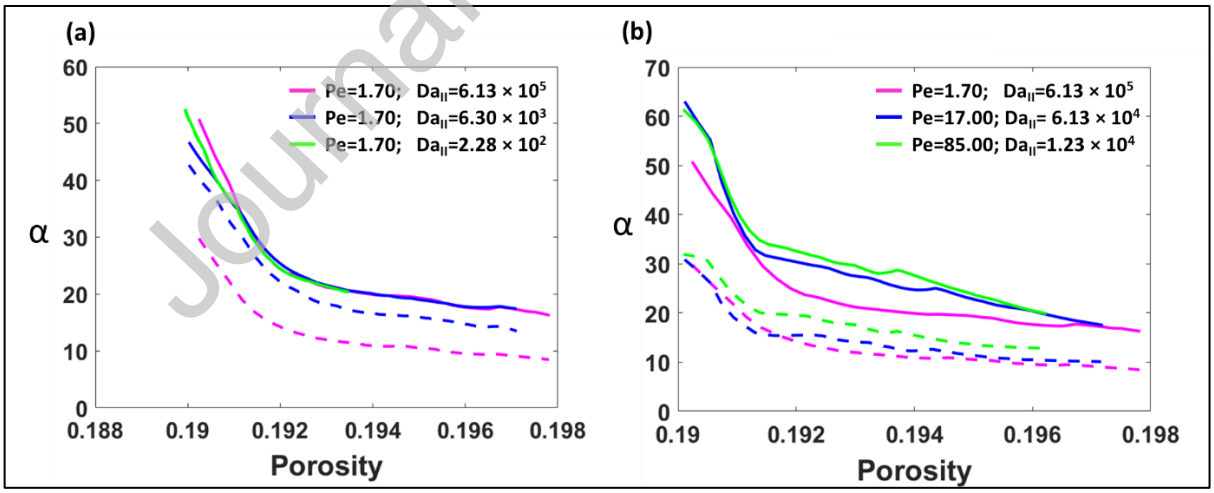

Figure 9: the α coefficient in the permeability relation. Power law exponent coefficient α as a function of porosity change for simulations with **(a)** constant injection velocity (i.e., constant $\widetilde{Pe}$ number = 1.70) using different solution pH values, and **(b)** injection of a solution with a

constant pH value of 1.0 using three different velocities. Note that the solid lines correspond to rtPNM and the dotted lines correspond to nrtPNM.

5. CONCLUSIONS

In the context of reactive pore network models for calcite dissolution, we have presented new constitutive relations to update pore throat conductance, which takes care of the evolving pore throat shape as per the imposed flow and reaction regimes. This was achieved through numerical simulation of reactive transport processes on a scale of single capillary/pore throat and later extraction of the evolution of conductance of the capillary. We observed that, for the advection dominated and reaction-controlled dissolution regimes, the conductance can be updated using the Hagen-Poiseuille relation, since the initial cylindrical pore throat shape is maintained during dissolution. On the contrary, for the diffusion dominated and reaction-dominated dissolution regimes, the pore throat shape changes to the half-hyperboloid (i.e., conical) shape and the proposed new conductance relations provides an improved description of the impact on conductance evolution of the pore throat.

Next, the derived conductance relations were implemented in pore network simulations and the prediction of permeability was compared with the existing pore network models. We observed that corresponding to the micro-CT experimental conditions i.e., $\widetilde{Pe}$=974, $\widetilde{Da_{II}}$=59.8 and $\widetilde{Pe}$=192, $\widetilde{Da_{II}}$=303, only around 11% of total pore throats were subjected to the conditions which are responsible for the development of the non-uniform pore throat shapes. Consequently, estimated permeability from the pore network model remained indifferent to the relations used for updating of conductance of individual pore throats. As a result, new and existing PNM provided equally good agreement with the permeability of the reacted sample image obtained after the experiment.

Finally, we performed a sensitivity study of the new conductance relations across a range of flow and reaction regimes. This revealed that the injection of highly acidic solutions with a pH value of 1.0 and at an injection velocity of 3.17×10^{-6} $m.s^{-1}$ caused 60% of total pore throats to modify their initially cylindrical shapes into non-uniform shapes due to dissolution. We observed that, compared to the newly modified PNM, utilization of existing PNM can lead to an overestimation of 27% in the predicted permeability value and an overestimation of over 50% in the fitted exponent α used in the porosity-permeability relationship. In the context of applications such as the injection of CO_2 or acidic solution into carbonate rocks, pore network models are the most promising tool for the prediction of porosity-permeability relations at the representative elementary volume level. Depending on the reactive-flow regime, incorporation of the dissolution induced changes of the pore throat shape may be required in order to enhance the prediction capacity of existing pore network models and possibly bring the modeled outcomes closer to field observations, for example, realistic prediction of porosity permeability changes in the case of development of different dissolution patterns when varied range of injection velocity or solution chemistry are utilized. In summary, PNM provide constitutive relations for REV's in continuum models that can be used to simulate field sites and we proposed improved constitutive relationships.

Declaration of competing interest

The authors declare that they have no known competing financial interests or personal relationships that could have appeared to influence the work reported in this paper.

Conflict of Interest and Authorship Conformation Form

- ✓ All authors have participated in (a) conception and design, or analysis and interpretation of the data; (b) drafting the article or revising it critically for important intellectual content; and (c) approval of the final version.

Acknowledgements

The research work of P.A., M.W. and A.R is part of the Industrial Partnership Programme i32 Computational Sciences for Energy Research that is carried out under an agreement between Shell and the Netherlands Organization for Scientific Research (NWO). M.W. has received funding from the European Research Council (ERC) under the European Union's Horizon 2020 research and innovation programme (grant agreement No. [819588]). The XMT experiments in this work were performed at Ghent University's Centre for X-ray Tomography (UGCT), a Centre of Expertise funded by the Ghent University Special Research Fund (BOF-UGent) under grant BOF.EXP.2017.007. TB, AM and VC received funding from the Research Foundation–Flanders (FWO) under project grant G051418N. TB is a postdoctoral fellow of the Research Foundation-Flanders (FWO) and acknowledges its support under Grant 12X0919N.

SUPPORTING INFORMATION AVAILABLE

Additional details on the presented results, tables 1-3 and figures 1-13.

REFERENCES

Acharya, R.C., Van Der Zee, S.E.A.T.M., Leijnse, A., 2005. Transport modeling of nonlinearly adsorbing solutes in physically heterogeneous pore networks. Water Resour. Res. 41, 1–11.

Agrawal, P., Raoof, A., Iliev, O., Wolthers, M., 2020. Evolution of pore-shape and its impact on pore conductivity during CO2 injection in calcite: Single pore simulations and microfluidic experiments. Adv. Water Resour. 136.

Al-Ameri, A., Gamadi, T., 2020. Optimization of acid fracturing for a tight carbonate reservoir. Petroleum 6, 70–79.

Al-Gharbi, M.S., Blunt, M.J., 2005. Dynamic network modeling of two-phase drainage in

porous media. Phys. Rev. E - Stat. Nonlinear, Soft Matter Phys. 71, 1–16.

Aslannejad, H., Fathi, H., Hassanizadeh, S.M., Raoof, A., Tomozeiu, N., 2018. Movement of a liquid droplet within a fibrous layer: Direct pore-scale modeling and experimental observations. Chem. Eng. Sci. 191, 78–86.

Bedram, A., Moosavi, A., 2011. Droplet breakup in an asymmetric microfluidic T junction. Eur. Phys. J. E 34.

Bernabé, Y., Mok, U., Evans, B., 2003. Permeability-porosity Relationships in Rocks Subjected to Various Evolution Processes. Pure Appl. Geophys. 160, 937–960.

Boever, W. De, Bultreys, T., Derluyn, H., Hoorebeke, L. Van, Cnudde, V., 2016. Comparison between traditional laboratory tests, permeability measurements and CT-based fluid flow modelling for cultural heritage applications. Sci. Total Environ. 554–555, 102–112..

Bultreys, T., Boone, M.A., Boone, M.N., De Schryver, T., Masschaele, B., Van Hoorebeke, L., Cnudde, V., 2016. Fast laboratory-based micro-computed tomography for pore-scale research: Illustrative experiments and perspectives on the future. Adv. Water Resour. 95, 341–351.

Ghanbarian B., Hunt A. G., D.H., 2016. Fluid flow in porous media with rough pore-solid interface. Water Resour. Res. 5, 2–2.

Golfier, F., Zarcone, C., Bazin, B., Lenormand, R., Lasseux, D., Quintard, M., 2002. On the ability of a Darcy-scale model to capture wormhole formation during the dissolution of a porous medium. J. Fluid Mech. 457, 213–254.

Hoefner, M.L., Fogler, H.S., 1988. Pore evolution and channel formation during flow and reaction in porous media. AIChE J. 34, 45–54.

Hommel, J., Coltman, E., Class, H., 2018. Porosity–Permeability Relations for Evolving Pore Space: A Review with a Focus on (Bio-)geochemically Altered Porous Media. Transp. Porous

Janbumrung, V., Trisarn, K., 2017. Acid Stimulation of Carbonate Reservoir in Northeastern Thailand Using Developed Computer Program. Int. J. Comput. 25, 40–51.

Leong, V.H., Ben Mahmud, H., 2019. A preliminary screening and characterization of suitable acids for sandstone matrix acidizing technique: a comprehensive review. J. Pet. Explor. Prod. Technol. 9, 753–778.

Li, L., Steefel, C.I., Yang, L., 2008. Scale dependence of mineral dissolution rates within single pores and fractures. Geochim. Cosmochim. Acta 72, 360–377.

Luquot, L., Gouze, P., 2009. Experimental determination of porosity and permeability changes induced by injection of CO2 into carbonate rocks. Chem. Geol. 265, 148–159.

Luquot, L., Rodriguez, O., Gouze, P., 2014. Experimental Characterization of Porosity Structure and Transport Property Changes in Limestone Undergoing Different Dissolution Regimes. Transp Porous Med 101, 507–532.

Mehmani, Y., Sun, T., Balhoff, M.T., Eichhubl, P., Bryant, · S, Bryant, S., 2012. Multiblock Pore-Scale Modeling and Upscaling of Reactive Transport: Application to Carbon Sequestration. Transp Porous Med 95, 305–326.

Meile, C., Tuncay, K., 2006. Scale dependence of reaction rates in porous media. Adv. Water Resour. 29, 62–71.

Menke, H.P., Bijeljic, B., Blunt, M.J., 2017. Dynamic reservoir-condition microtomography of reactive transport in complex carbonates: Effect of initial pore structure and initial brine pH. Geochim. Cosmochim. Acta 204, 267–285.

Molins, S., Trebotich, D., Yang, L., Ajo-Franklin, J.B., Ligocki, T.J., Shen, C., Steefel, C.I., 2014. Pore-scale controls on calcite dissolution rates from flow-through laboratory and numerical experiments. Environ. Sci. Technol. 48, 7453–7460.

Nogues, J.P., Fitts, J.P., Celia, M.A., Peters, C.A., 2013. Permeability evolution due to dissolution and precipitation of carbonates using reactive transport modeling in pore networks. Water Resour. Res. 49, 6006–6021.

Parkhurst, D., Appelo, C., 2013. Description of Input and Examples for PHREEQC Version 3—A Computer Program for Speciation, Batch-Reaction, One-Dimensional Transport, and Inverse Geochemical Calculations.

Parvan, A., Jafari, S., Rahnama, M., Norouzi apourvari, S., Raoof, A., 2020. Insight into particle retention and clogging in porous media; a pore scale study using lattice Boltzmann method. Adv. Water Resour. 138, 103530.

Plummer, L. N.; Wigley, T. M. L., 1978. Parkhurst, D. L. The kinetics of calcite dissolution in CO2-water systems at 5°C to 60°C and 0.0 to 1.0 atm CO_2. Am. J. Sci. 278, 179–216.

Plummer, L.N., Busenberg, E., 1982. The solubilities of calcite, aragonite, and vaterite in carbon dioxide-water solutions between 0 and 90°C, and an evaluation of the aqueous model for the system calcium carbonate-carbon dioxide-water. Geochim. Cosmochim. Acta 46, 1011–1040.

Raeini, A.Q., Bijeljic, B., Blunt, M.J., 2017. Generalized network modeling: Network extraction as a coarse-scale discretization of the void space of porous media. Phys. Rev. E 96, 1–17.

Raoof, A., Hassanizadeh, S.M., 2012. A new formulation for pore-network modeling of two-phase flow. Water Resour. Res. 48, 1–13.

Raoof, A., Hassanizadeh, S.M., 2009. A new method for generating pore-network models of porous media. Transp. Porous Media 81, 391–407.

Raoof, A., Nick, H.M., Hassanizadeh, S.M., Spiers, C.J., 2013. PoreFlow: A complex pore-network model for simulation of reactive transport in variably saturated porous media. Comput. Geosci. 61, 160–174.

Raoof, A., Nick, H.M., Wolterbeek, T.K.T., Spiers, C.J., 2012. Pore-scale modeling of reactive transport in wellbore cement under CO2 storage conditions. Int. J. Greenh. Gas Control 11, 67–77.

Vlassenbroeck, J., Dierick, M., Masschaele, B., Cnudde, V., Van Hoorebeke, L., Jacobs, P., 2007. Software tools for quantification of X-ray microtomography at the UGCT. Nucl. Instruments Methods Phys. Res. Sect. A Accel. Spectrometers, Detect. Assoc. Equip. 580, 442–445.